

Spatially Resolved Spectrometry of Laser-Ionized Matter

A thesis submitted in partial fulfillment of the requirement
for the degree of Bachelor of Science with Honors in
Physics from the College of William and Mary in Virginia,

by

Peter John de Castro

Accepted for _____ Honors

Advisor: Dr. Jan Chaloupka

Dr. John Delos

Dr. William Kossler

Dr. Evan Feldman

Williamsburg, Virginia
May 2006

Abstract

Rescattering is a proposed mechanism for non-sequential ionization of atoms by high intensity light sources such as lasers. The phenomenon has been studied in detail at very high laser intensities, but low-intensity studies suffer from poor statistics. This is due to the low repetition rate of traditional tabletop lasers and the inherently low ionization rates at these lower intensities. We propose a new experimental setup to allow for ultra-high repetition rate studies in the previously inaccessible low-intensity regime. A novel ion spectrometer for use at high repetition rates has been designed and constructed.

Contents

1	Introduction and Theory.....	1
1.1	Single-Photon and Multiphoton Ionization.....	1
1.2	Rescattering.....	3
1.3	Experiments and Limitations.....	6
1.4	Proposal.....	7
2	Spectrometer Design, Construction, and Testing.....	9
2.1	Design Considerations.....	9
2.2	Virtual Construction.....	10
2.3	Simulation.....	15
3	Results.....	17
3.1	Spectrometer Construction and Testing.....	17
3.2	Laser Amplification System.....	20
3.3	Ion Detection Testing.....	21
4	Future Work and Conclusion.....	22
4.1	Electrostatic Deflection.....	22
4.2	Ion Optics.....	23
4.3	Conclusion.....	25

1 Introduction and Theory

1.1 Single-Photon and Multiphoton Ionization

Ionization can occur by several mechanisms when an atom is exposed to an external electric field. One of these mechanisms is the photoelectric effect, where a single photon of sufficiently high frequency can free an electron. To determine the threshold frequency, one needs to equate the ionization energy E to the photon energy $h\nu$, where h is Planck's constant, and ν is the photon frequency.

$$E = h\nu \quad (1)$$

From this, we can see that

$$\nu = \frac{E}{h} \quad (2)$$

For helium, this means that a photon of frequency

$$\nu = \frac{E}{h} = \frac{3.939 \times 10^{-18} \text{ J}}{6.626 \times 10^{-34} \text{ J}\cdot\text{s}} = 5.945 \times 10^{15} \text{ Hz} \quad (3)$$

(50nm ultraviolet light) or higher is required for ionization. If a photon with a higher frequency than is necessary for ionization is absorbed, the excess energy will be converted into kinetic energy in the ejected electron.

If the individual photon energy in a particular light source is lower than the ionization energy, this model alone suggests that no ionization can occur. However, it has been shown that electrons may be freed by an atom by absorbing multiple low-energy photons simultaneously [1,2]. The energy absorbed is simply the sum of the individual

absorbed photon energies. Ionization in this way can be reproduced reliably using high-intensity lasers. Another useful picture of this strong-field ionization effect is a combination of a classical field picture and quantum tunneling. In this perspective, an applied electric field distorts the Coulomb potential of the atom's nucleus, creating a distorted Coulomb potential, shown as the thick black line in Figure 1. The higher the applied field, the better the chance that an electron will tunnel through the potential barrier (in the positive x direction in Figure 1) and be liberated. If the field is high enough, the potential barrier to the right in Figure 1 will be so low that the electron can escape in a classical sense without tunneling. Again, these effects can be observed when a high-intensity laser is used to provide the external field.

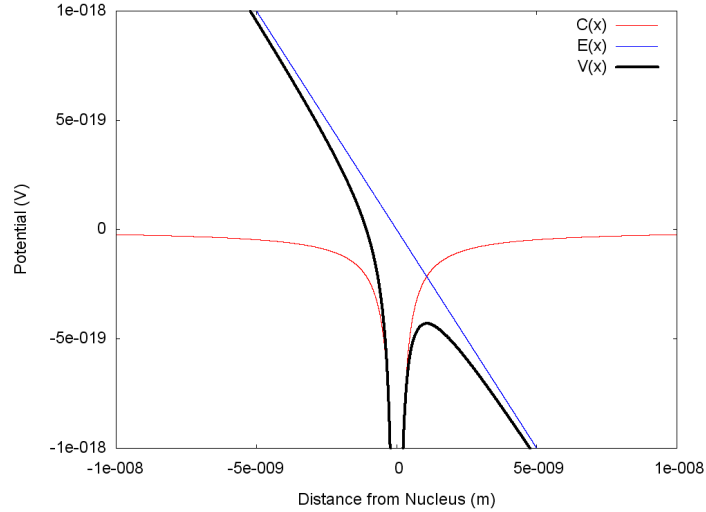


Figure 1: The Coulomb potential $C(x)$, an applied field's potential $E(x)$, and their superposition $V(x)$. Scales chosen for conceptual clarity.

The validity of these two strong-field pictures is determined by the Keldysh, or adiabaticity, parameter [14]. This is defined as

$$\gamma = \sqrt{\frac{I_p}{2U_p}} \quad , \quad (4)$$

where I_p is the ionization potential and U_p is the ponderomotive potential (an effective time-averaged potential felt by an electron in the laser's AC electric field that varies proportionally to the square of the laser wavelength and linearly with the intensity.) If U_p is large compared to I_p , that is, if the laser is oscillating at a slow rate with respect to the natural electron movements in the atom, then γ is small, and the semi-classical tunneling picture is valid. In this case, the distorted potential can be considered quasi-static. In the case of large γ , the laser field is changing quickly with respect to electron motion, so a multiphoton picture must be used. Xenon has a single-ionization potential of 12.1 eV. When exposed to one-half of its single-ionization saturation intensity ($\frac{1}{2}I_{\text{sat}} = 45 \text{ TW/cm}^2$), a free electron feels a ponderomotive potential of 2.55 eV. The resulting Keldysh parameter is equal to 1.5, placing this process in the multiphoton regime. In contrast, helium has a single-ionization potential of 24.6 eV. At an intensity of 400 TW/cm^2 (equal to its $\frac{1}{2}I_{\text{sat}}$), the ponderomotive potential is equal to 22.5 eV, resulting in a Keldysh parameter of 0.7. This puts the ionization of helium (with 800nm light) into the semi-classical tunneling regime. As a result, studying the dynamics of helium ionization is an excellent way to probe the limits of the semi-classical descriptions of strong-field laser-atom interaction.

1.2 Rescattering

The multiphoton and tunneling mechanisms on their own are very good at explaining the liberation of single electrons. However, explaining multiple ionization needs a more sophisticated approach. Any remaining electrons lose the Coulombic "shielding" formerly provided by the freed electron. Because of this, the remaining electrons require a significant amount more energy to be sequentially ionized, where multiple electrons removed, each by their own photoionization event. As a concrete example, the first ionization of helium occurs at 24.6eV, and the second occurs at 54.4eV [5]. This second ionization energy corresponds to that of a photon of wavelength 22nm, utilizing eq.2.

Based solely on single-photon and multiphoton models, helium may be doubly ionized by imparting 24.6eV and then 54.4eV to it.

However, experiments show that double ionization occurs at rates three orders of magnitude greater than those predicted by sequential ionization theory [4,6,8,11] for low intensities. In these experiments, double ionization of helium occurs at surprisingly high rates using a pulsed 800nm laser at an intensity of approximately 0.1 PW/cm².

Sequential ionization theory, on the other hand, does not predict these high rates until the laser intensity has been increased by an order of magnitude. Figure 2 shows the single ionization counts of ⁴He with respect to laser intensity as the upper set of black squares. The lower set of black squares represents the counts of doubly ionized ⁴He. The right edge of the shaded gray area shows the prediction made by sequential ionization theory, and it clearly underestimates the experimental results. The same effect follows with ³He, whose double ionization counts are represented by open circles. The results of this and similar experiments reveal the need to investigate other mechanisms.

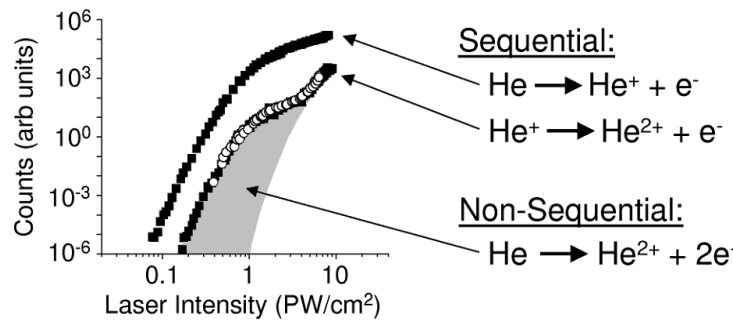


Figure 2: Single and double ionization yields curves as a function of laser intensity. Image from [6].

One proposed mechanism that shows excellent correlation between experiment and theory is rescattering [7]. When the laser field ionizes an atom classically or through tunneling as in Figure 1, the freed electron may escape completely and never return, or it may be driven back toward the nucleus after the laser field has reversed direction. This

returning electron may collide with a second electron still bound to the nucleus, and – if it has gained enough energy from the laser on the return trip – it may free the second electron, resulting in double ionization [3] as depicted in Figure 3.

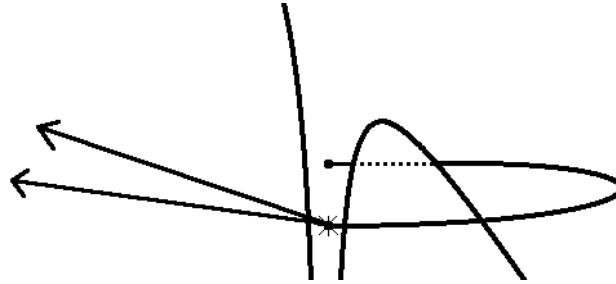


Figure 3: Conceptual illustration of the initial distorted Coulomb potential and the rescattering trajectories. The first electron escapes by tunneling, then, as the laser field oscillates, it returns to the atom. Finally, it imparts enough energy to a second electron so that they are both freed.

The chance of double ionization therefore depends greatly on the timing of the first ionization and the position of the atom within the laser focus at the time of that event. If the electron is liberated at a null of the laser field, it will gain a large kinetic energy, but it will not be driven back to the parent ion. If it is released at the peak of the field, it will reencounter the parent ion but with no kinetic energy. At a phase of 17 degrees after the peak of the field, it will impact the ion with a maximum kinetic energy of $3.2U_p$. William and Mary graduate student Jay Paquette is currently working on a simulation to more accurately determine how the timing and positioning of the ionization events affect the chance of rescattering.

1.3 Experiments and Limitations

Recent experiments [4,6,8] have used time-of-flight and coincidence techniques to investigate the non-sequential double ionization mechanisms for different ions, such as He^+ and He^{2+} . The researchers used a vacuum chamber backfilled with a gas to a pressure that will yield roughly one ion per laser pulse at a given intensity. After a pulse, the electron(s) are allowed to drift down a field-free tube toward the electron detector. During this drift time, several plates perpendicular to the flight axis are set to different potentials, such that the ions are accelerated toward a detector at the opposite end of the chamber. The ions' and electrons' flight times are recorded and used to determine their charge and energies, respectively, and another pulse follows on the order of 1msec later. During analysis, the ratios of different ion species are compared to the laser intensity for that segment of the experiment to show contributions of different effects to the total double-ionization event probability. They also use the electron energy spectra to gain further insight into the phenomena.

While these and other experiments have shown good evidence to support rescattering, they all share one drawback. Being time-of-flight experiments, if the laser is pulsed more frequently than the time it takes ions to travel to the detector, there would be no way to tell which pulse a detected ion came from. Flight times are on the order of $10\mu\text{sec}$ for ions, and the laser pulses are spaced 1msec apart, so the vast majority of time is spent waiting for ions to travel to the detector instead of creating ions. When the experiments are run on the order of $0.1 \text{ PW}/\text{cm}^2$, double ionization becomes extremely rare. This rarity of events combined with the long wait between laser pulses makes it impractical to try to gather statistics at these low intensities. Unfortunately, this low-intensity range is also where the rescattering model will face its most severe test. Lower intensities result in ejected electrons not being able to gain enough energy from the laser on their return trip to liberate a second electron, and the multiphoton picture must be used to describe any ionization that occurs. To better understand this transition between the tunneling and multiphoton regimes, ion yield data at low intensities must be gathered.

1.4 Proposal

We propose an experiment free from the restrictions of TOF techniques. As in the previously described experiments, an ultra-high vacuum (UHV) chamber (about 10^{-9} Torr) will be back-filled with the gas to be studied (*e.g.* ^3He , Ne, Ar, Kr, or Xe), and the gas will be ionized by a pulsed laser passing through the side of the chamber and focused at the chamber's center. Two electrically isolated plates mounted perpendicular to the chamber walls will be held at different potentials so that the ions are accelerated toward the detector. The plate closest to the detector will have a hole in its center to allow the ions to pass through. Variants of this basic setup have been used successfully in the previously mentioned TOF experiments. However, instead of timing the flights of each ion to determine its species, our experiment will use a magnetic field to separate them spatially and a microchannel plate (MCP) with a phosphor screen to detect them. This concept is illustrated in Figure 4, and a simulation done with the industry-standard program SimIon [13] has been performed to support it. The simulation and program are both explained in greater detail in section 2.3.

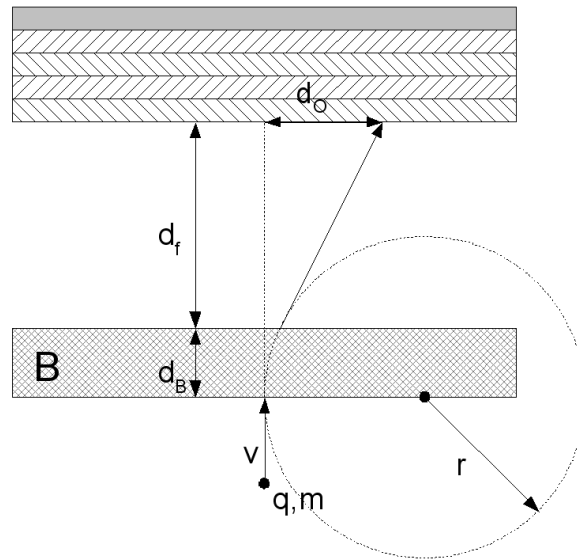


Figure 4: Schematic setup of the magnetic deflection portion of the experiment.

Assuming a uniform magnetic field B , the distance d_o the ions will be offset from the axis of the flight tube is found to be

$$d_o = \frac{d_f + d_B}{\sqrt{\left(\frac{r}{d_B}\right)^2 - 1}} \quad (5)$$

where d_f is the distance from the end of the magnetic field region to the detector, d_B is the width of the magnetic field region, and r is the cyclotron radius of the ion, given by

$$r = \frac{mv}{qB} \quad (6)$$

where m , v , and q are its mass, speed, and charge, respectively. The only parameters that differ significantly between ion species are the net charge q and the flight velocity v ; hence the spatial separation by species at the detector. Between ionic species of the same atom, the mass m varies only by the number of liberated electrons, so its impact on d_o is negligible. For a physical example, we will set

$$\begin{aligned} d_f &= 0.064 \text{ m} \\ d_B &= 0.025 \text{ m} \\ m &= 5.020 \times 10^{-27} \text{ kg} \\ B &= 0.023 \text{ T} \\ q^+ &= 1.602 \times 10^{-19} \text{ C} \\ q^{2+} &= 3.204 \times 10^{-19} \text{ C} \\ v^+ &= 2.526 \times 10^5 \text{ m/sec} \\ v^{2+} &= 3.573 \times 10^5 \text{ m/sec} \end{aligned} \quad (7a-h)$$

for the case of ^3He , and where the "+" and "2+" superscripts differentiate between variables for the two ion species. The ions are assumed to start at rest, and their velocities are due to an acceleration across a 500V potential drop to ground. These

parameters yield $d_o^+=0.919\text{cm}$ and $d_o^{2+}=1.307\text{cm}$. That means that we will see a separation of ion species by about 0.388cm for ${}^3\text{He}$. In the event that stray fields cause a distribution of d_o values that brings different species within range of each other at the detector, an increase of the separating magnetic field, an increase of d_f , or a decrease of the extraction voltage increases the inter-species separation at the detector.

With this technique, we will be able to correlate the probability of obtaining multiple ionization with the laser intensity. More significantly, owing to the spatially-resolved nature of the experiment, we can attempt as many ionizations as desired while the ions travel the length of the chamber. The only limits to the repetition rate are the detector response time, the time required for ionization products to exit the laser focus, and the repetition rate of the laser system. MCPs and phosphor screens both have typical response times on the order of 10ns or less, setting the limit to at least 100MHz . Assuming a $5\mu\text{m}$ laser focus and an extraction field of approximately 8V/m given by a voltage of 1kV across $0.5''$, all of which are reasonable experimental parameters, ${}^{130}\text{Xe}^+$ leaves the laser focus on the order of 10nsec , so the limit remains at 100MHz , even for a heavy atom such as xenon. With the use of a light source such as the free electron laser (FEL) at the Thomas Jefferson National Accelerator Facility (JLab), repetition rates up to 75MHz are currently attainable. Using the technique described in this paper, we will be able to take full advantage of this high repetition rate, yielding a dataset more than four orders of magnitude larger in a given time span than in previous experiments.

2 Spectrometer Design, Construction, and Testing

2.1 Design Considerations

The ion detector consists of a micro-channel plate (MCP) coupled to a phosphor screen. Charged particles enter small channels in the plate and create a cascade of electrons down

progressively higher potentials (in much the same way as a photomultiplier tube.) The resulting group of electrons impacts the phosphor screen and creates a flash of light that can be observed by various means, such as a CCD camera or photodiode. This results in extreme sensitivity with very good spatial resolution.

The MCP to be used has a spatial resolution on the order of 10 microns. Since we will be creating separation between species on the order of centimeters, the detector resolution presents no problems. Also, the desired magnetic field is easily attainable using commercially available neodymium magnets or an electromagnet. The vacuum chamber is about 4 inches in diameter and in its current configuration presents a 13" flight path. As shown above in the physical deflection example, this is more than enough space to allow for ample spatial separation of He ions. To increase the rigidity of the apparatus as well as to minimize interference from stray electric fields, the plates and other parts will be mounted inside an aluminum tube which will then be inserted into the vacuum chamber. To attenuate external magnetic interference as much as possible, high magnetic permeability mu-metal foil is wrapped around the vacuum chamber flight tube [16].

The goal of the design process for this experiment was to create an assembly that would be easy to build and adjust, and at the same time be rigid to accommodate accurate ion trajectories and consistent results. The inner diameter of the chamber also put restrictions on the size and complexity of the apparatus.

2.2 Virtual Construction

Blender is an open-source program that allows its user to create three-dimensional models and do many other tasks associated with computer-based imaging [12]. While it's not specifically designed with practical CAD (computer-aided design) applications in mind, it can be a valuable tool for design and visualization purposes. It was used here to design the apparatus for the experiment and to test several ideas that would have been difficult to represent on paper.

Keeping simplicity and rigidity in mind, the first design (Figure 5) saw the electric and magnetic shields as lipped cylinders stacked inside each other. An aluminum ring on top of these supported threaded rods off of which would hang the extraction and deflection assemblies. This design was indeed very modular, and it was physically simple and rigid as far as the shields were concerned, allowing the rest of the apparatus to move freely at the lower end. However, it would have been difficult to weld the lips at exactly 90 degrees to the shields. Since the shield walls needed to be as close to the chamber walls as possible to leave enough space for the components inside, a non-perpendicular weld would have made it very difficult or impossible to insert the shields into the chamber. Additionally, welding components for UHV use requires great care, as even small voids will generate "virtual leaks."

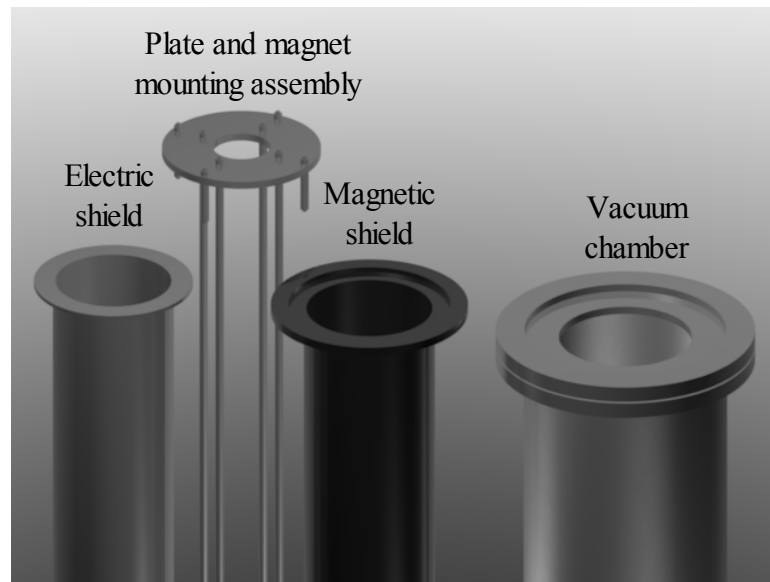


Figure 5: The first spectrometer design. The pieces were designed to neatly stack inside each other.

The next design, shown in Figure 6, sought to fix the practicality and rigidity flaws of the previous one. The shields became simple cylinders (yellow and red), fitting into concentric circular slots on two aluminum rings (purple.) The top ring was bolted to

a flange (dark grey) at the right hand side of Figure 6. The rings attached to the outer shield with set screws, the inner shield rested in the rings' grooves, and the bottom ring prevented the four threaded rods (two shown in blue) from moving. This was a much more rigid design, but since the rings' slots would have been very difficult to machine, new shield mounting ideas were considered.

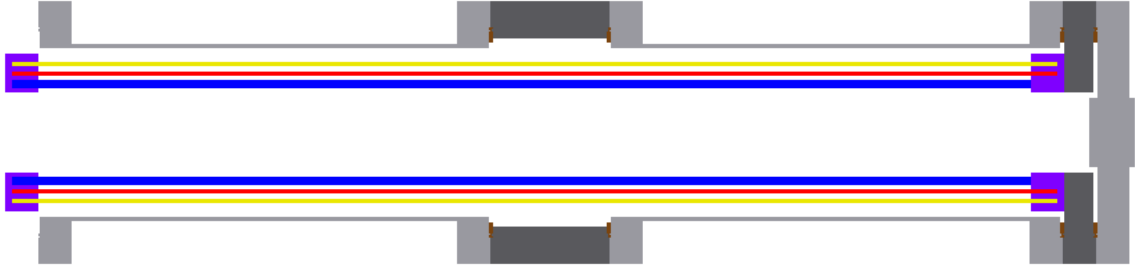


Figure 6: A cross-sectional view of the second spectrometer design. Rigidity was much improved, but a different fabrication problem was created.

The third design (Figure 7) was a result of the best of these shield mounting considerations. The threaded rods (red) screwed directly into the flange (dark gray), the magnetic shield would be a foil wrapped around the outside, and the electric shield (yellow) screwed into the inner and outer edges of an aluminum ring (purple) fastened to these rods. A set of shorter rods (black) would support the magnetic deflection assembly. This solved the shield mounting problem while preserving the rigidity of the second design, but the flange became too crowded to fit everything, or else it would have had to block part of the detector.

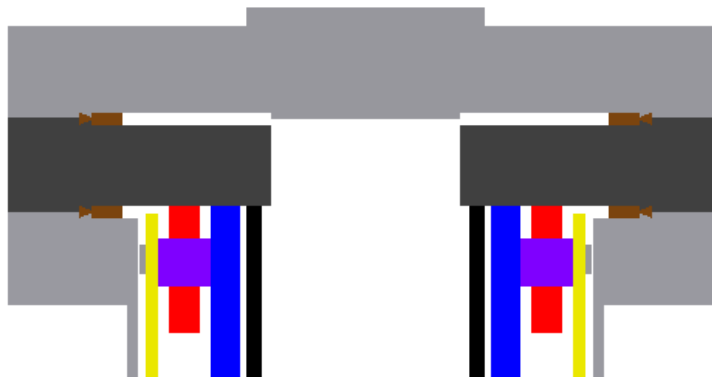


Figure 7: The third spectrometer design. This shows a close-up cross-sectional view of the new mounting scheme.

The fourth design used the shield mounting idea from the third design and simplified the rest of the mounting setup. Instead of separate rods for mounting the shields, extraction plates, and magnets, a single set of four threaded rods (the two horizontal, dark gray lines in Figure 8) supported the rings on which the electric shield was mounted. Additionally, two rings were introduced toward the center (light gray rectangles) for supporting the extraction plates. These two middle rings held alumina rods (Al_2O_3 , shown in red) on which the extraction plates were mounted to keep them electrically insulated from each other.

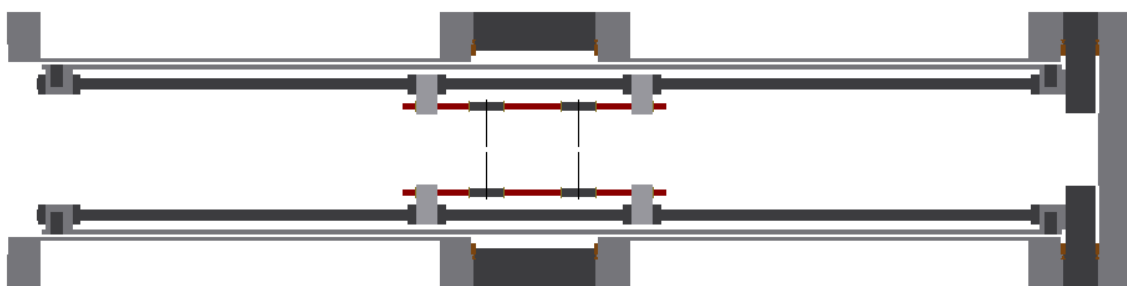


Figure 8: The fourth spectrometer design. Apparatus became simpler, more rigid, and less crowded.

The fifth design consists mostly of tweaks to the fourth before finalizing it and ordering the parts and machining work. The dimensions of all four rings and the shield have changed slightly to accommodate the size of tubes available for shielding and to fit inside the welding spots on the inside of the chamber. This final design shown in Figure 9a,b is easy to modify and is very rigid. The cross-sectional view in Figure 9a shows how all the parts are arranged once assembled. Figure 9b shows the spectrometer in its entirety, separated into three sections. The extraction and support assembly (left) is inserted into the electric shielding tube (center), and those parts are then inserted into the vacuum chamber (right) with the MCP attached.

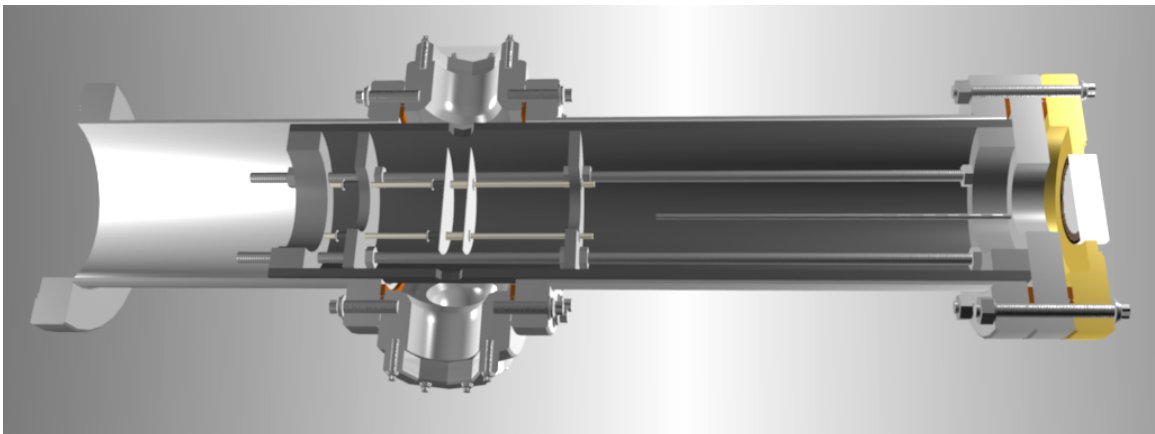


Figure 9a: The final and final spectrometer design, shown in cross-section.

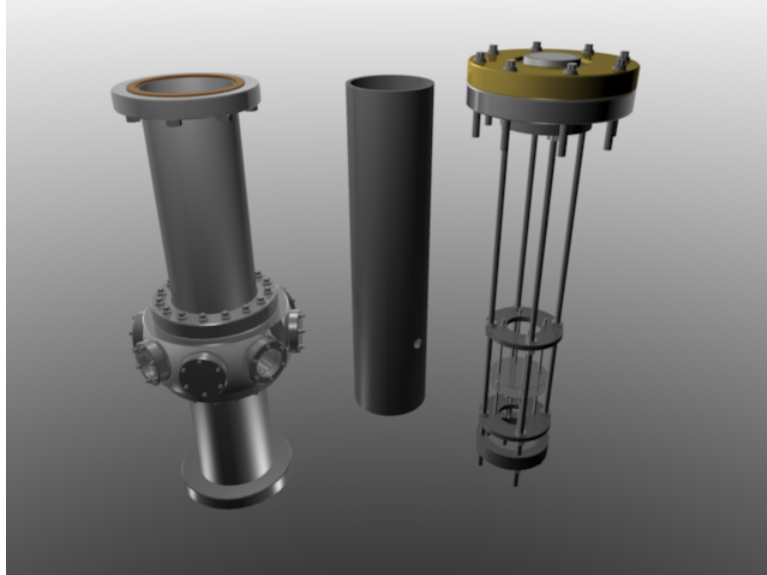


Figure 9b: A full view of the final design. Figure 11 shows a similar view of the physical apparatus.

2.3 Simulation

SimIon is an industry-standard program used to simulate the movement of charged and neutral particles in a static or dynamic electromagnetic environment [13]. It uses a finite-element model for the experiment's components, which means that the apparatus is defined by marking points on a three-dimensional grid as free space, electrodes, or magnetic "pole points". The Laplace equation is applied to interpolate field values from electrode elements. This results in a field model for the entire experiment that is very accurate unless you get very close to (one or two grid points away) a curved surface, which, due to the nature of the model, is represented by a coarse surface approximating the desired curve. Particles in the simulation may have independent charges, masses, and initial positions and trajectories. In the simulation's default visualization, the experiment's structure is represented by a brown grid, and ion paths are traced out in black.

The final design was converted to a SimIon model ("potential array"), including the shielding, extraction plates, magnets, and the mounting rings. Initial ion velocities were set to zero. The shielding and rings were treated as grounded electrodes, as was the extraction plate closest to the MCP. The plate furthest from the MCP was set to 1kV, and the magnets were given a 60 "mag" field value. Using two 1" diameter, 0.25" high cylindrical magnets with 0.5" of space between them, the resulting field along the ion flight path was 230 ± 5 Gauss. The centers of the magnets were positioned 10" from the midpoint between the extraction plates and 3" from the MCP in order to give the largest separation of species while keeping them in the detector's active area. This configuration resulted in ${}^3\text{He}^+$ moving 1.244cm and ${}^3\text{He}^{2+}$ moving 1.759cm from the chamber's axis. That translates to a separation between species of 0.516cm, and the dispersion of ions born up to 0.00254cm apart resulted in impact sites no more than 0.05cm wide. The visualization of this simulation is shown in Figure 10. The extraction plates are not visible since they are less than one pixel wide at the figure's zoom level, but they are present in the calculation. The shield was not originally modeled to the correct length, but since the electric field was zero to one part in ten thousand, its remodeling was deemed unnecessary.



Figure 10: The SimIon simulation's visualization.

If we compare this to the theoretical result obtained earlier, which has the same parameters as this simulation, we see that the ions are displaced further from the axis and the species are better separated. This can be accounted for by the fact that a non-zero

magnetic field is present throughout the chamber, as in a real-world experiment, as opposed to the theoretical treatment's idealistic representation of a completely contained field. Since the magnetic field is present to varying degrees along the entire flight path, the deflection of the ions also occurs during their entire flight, not just a single inch of it.

3 Results

3.1 Spectrometer Construction and Testing

The vacuum chamber and MCP assembly had been purchased before the start of this project. All other parts were purchased based on the design process described earlier. The alumina rods, springs, clips, and spacers for the extraction assembly are all stock parts, but the threaded rods had to be shortened to fit in the chamber. The extraction plates were machined from a 0.02" stainless steel sheet. The electric shield was turned down from a stock aluminum pipe, the four mounting rings were machined from aluminum stock, and the double-sided stainless steel vacuum flange had a large hole bored in it to expose the MCP and small holes drilled and tapped in it for mounting the main threaded rods and magnet-mounting rods. Once the shield had been turned down to its final size, it was lowered into the chamber, the laser entrance and exit positions were marked on it using a high-power green laser, and holes were drilled out using the laser reference marks for alignment.

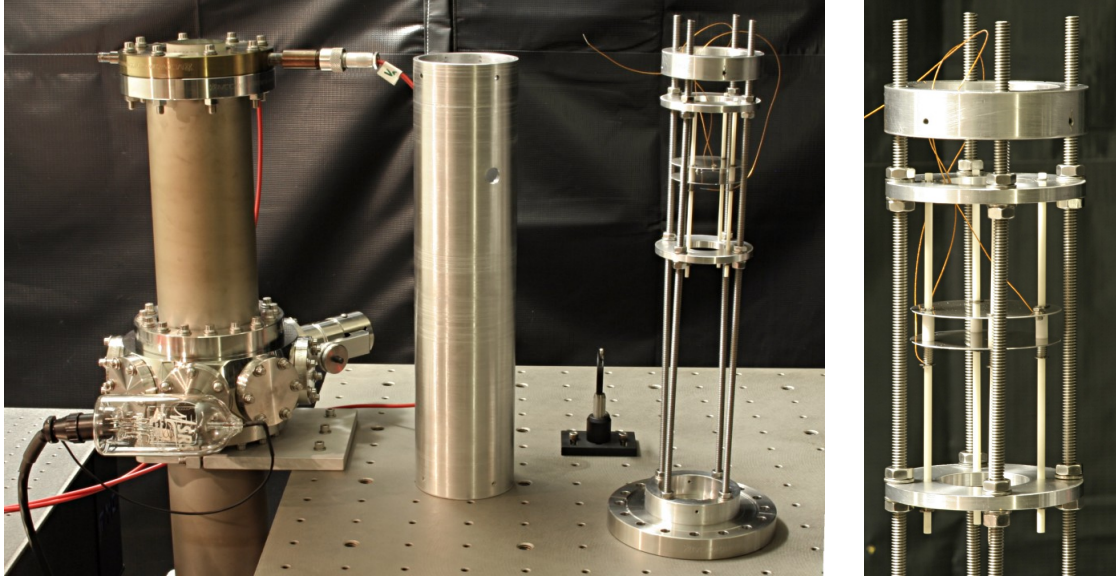


Figure 11a,b: The assembled spectrometer components (a) and a closeup of the extraction assembly (b).

With the final versions of all the pieces, the spectrometer is easy to assemble, though one needs to take care to ensure that the extraction plates are parallel to each other, perpendicular to the chamber's axis, and lined up with the windows in the shielding. The assembled spectrometer is shown above in Figure 11.

To measure the quality of the vacuum in the chamber, an ionization gauge is attached to the spherical octagon, the central part of the chamber named as such because of its eight exterior mounting points and spherical inner shape. The ionization gauge looks much like a light bulb (see Figure 11a) and works by ejecting electrons from a filament and collecting ions created by collisions between the electrons and atoms or molecules in the chamber. One fortunate side effect of operating this device is the generation of a large number of electrons flying about the chamber. When the MCP is turned on, many of these electrons are attracted to it and register events on the phosphor screen. This allows us to test the MCP's behavior. In particular, we have used these electrons to demonstrate the qualitative effectiveness of the magnetic shielding material. Two stacks of neodymium magnets were held in position by optics mounting stands at

opposite sides of the chamber, about half way up and 4.5" from the center of the flight tube. Their poles were oppositely oriented to maximize the field inside the chamber. Three pictures were then taken of the phosphor screen: one with a single sheet of magnetic shielding wrapped around the flight tube and separating it from the magnets, one without the shielding, and one with no magnets. The results are shown below in Figure 12. Since the electrons from the gauge have widely varying trajectories, a quantitative demonstration is not possible, but this test gives an indication of the degree to which charged particles can be shielded from magnetic fields by the magnetic shielding material. Figure 12 shows three 3.2-second exposures of the MCP. When the magnets were removed far enough from the chamber that they produced no noticeable effect on the display (b), a bright spot is seen in the middle of the MCP, surrounded by the glow from more rarefied impact sites. With the magnets present outside a single layer of shielding (a), the electrons experience some deflection, but high-probability impact sites can still be discerned. When the shielding is removed (c), the electrons are so severely diverted from the detector that there is almost no activity shown on the phosphor screen. Stray fields due to equipment in the lab and Earth's magnetic field are much weaker than the fields generated by these magnets.

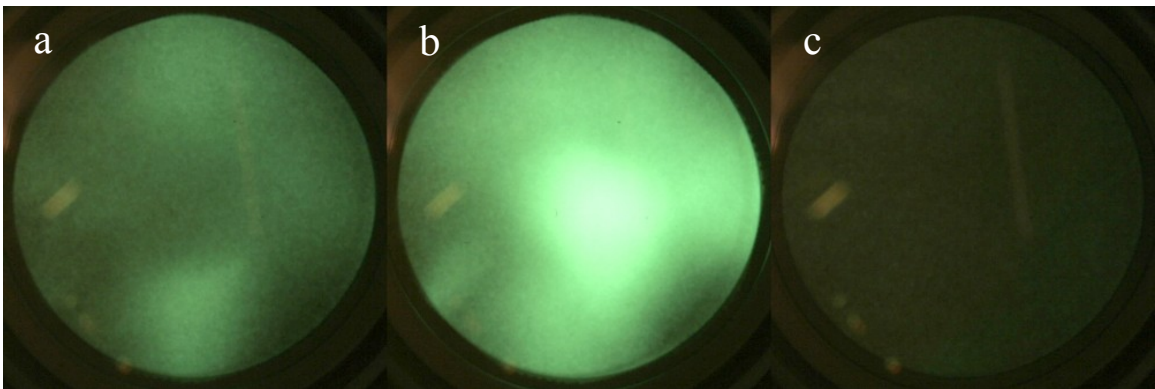


Figure 12a,b,c: Qualitative test of the magnetic shielding material with the MCP and electrons. From the left: magnets and one layer of shielding, no magnets, and magnets without any shielding.

As an example of how the shielding can protect precisely directed particles from being redirected by stray magnetic fields, a stack of neodymium magnets was held above the back of a cathode-ray tube (CRT) computer monitor, which functions by shooting electrons at a phosphor screen. In Figure 13, an image taken with neither magnets nor shielding is added to images taken with the magnets and (a) several layers of shielding around them, and (b) no shielding around them. This allows us to compare the shielded and unshielded cases with the magnet-free case, where the differences between them show up as a doubled or blurred image. From this, one can see that the shielding greatly attenuates the field deflecting the electrons in the CRT.

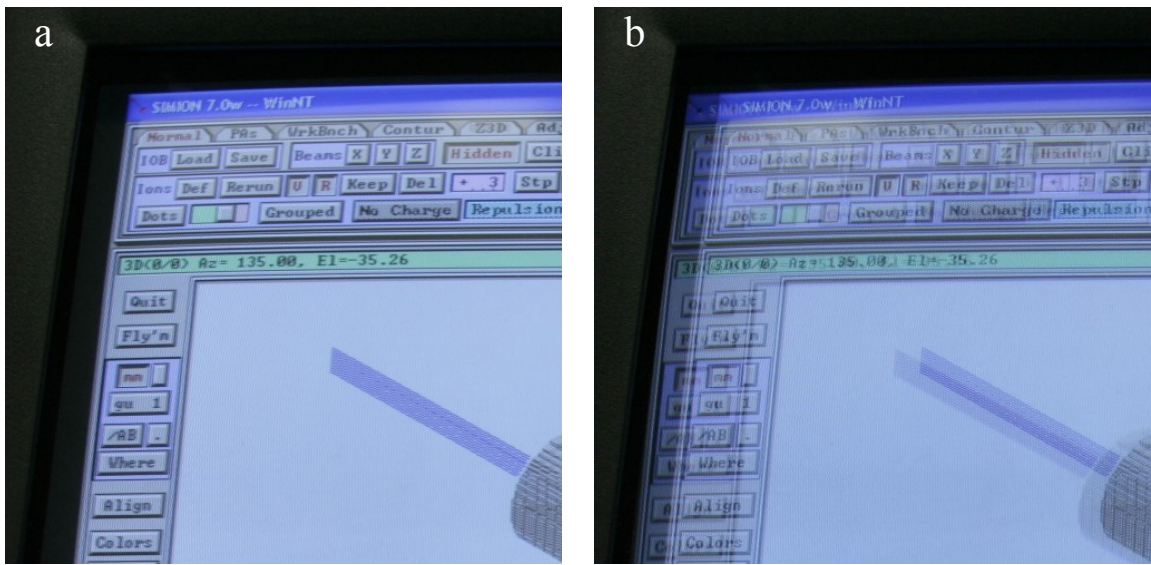


Figure 13a,b: Qualitative test of the magnetic shielding material with a CRT monitor. An image with no magnetic distortion was overlaid with ones taken with (a, left) shielded magnets and (b, right) unshielded magnets.

3.2 Laser Amplification System

An 800nm (infrared) oscillator with a repetition rate on the order of 100MHz and pulse widths on the order of femtoseconds is the light source to be amplified in a multipass

amplifier. The initial output of the oscillator is passed through a pulse-picker (a Pockel's cell, which rotates the polarization of one pulse in a train by 90 degrees, sandwiched between two crossed polarizers), reducing the repetition rate to 1kHz. Doing this makes it possible to have a series of pulses separated by 1msec, rather than restricting them to the 10nsec separation dictated by the oscillator. The pulses are then sent through a chirped-pulse stretcher, which spreads out each pulse in time according to its frequency components. The resultant progression of frequencies is what gives a pulse its "chirped" name. This process is necessary to prevent damage to the amplification components, since the peak intensity is reduced by the stretch factor. Once stretched, the pulse enters a cavity with spherical mirrors at its ends and a titanium:sapphire crystal in the center serving as the gain medium. The crystal is pumped by a pulsed 527nm (green) laser. The curved mirrors direct the pulse through the gain medium eight times before it exits the cavity, resulting in a gain of about 5^8 , or approximately 4×10^5 .

After the pulse leaves the amplification cavity, it is directed through a chirped-pulse compressor, which undoes the work done by the stretcher. This compresses each pulse in the train a thousand-fold, resulting in 1mJ, 50-fsec pulses at 1kHz. This intense pulse train is then directed toward the vacuum chamber where it is focused down to trigger ionization. For a focused spot with a $1/e^2$ -radius (w_0) of $5\mu\text{m}$, this results in a peak intensity of 25 PW/cm^2 .

3.3 Ion Detection Testing

Due to several unforeseen difficulties, initial results from the spatial separation of ion species are still pending. For part of the research period, there was difficulty aligning the laser amplification system. More recently, the absence of air conditioning in the building has prohibited the equipment from being run without risk of damage, so further tuning and subsequent usage has been impossible. This continues to be a problem in our lab and is being investigated.

Once we obtain proper amplification from the laser system, we will be able to create ions with the pulsed laser and presumably show their spatial separation into different species. Time-permitting, we will attempt to reproduce high-intensity results to confirm the spectrometer's capability.

4 Future Work and Conclusion

4.1 Electrostatic Deflection

After our device is seen to produce the expected results in the high-intensity range, it will be used to investigate the effects of strong-field ionization in the low-intensity regime. As was mentioned earlier, adjustments to the magnet strength, flight path length, and the extraction voltage can be made to increase the separation between ion species. This will be of particular importance for heavier targets such as xenon that will resist deflection more than helium.

However, deflection by magnets alone will eventually direct ions outside the active area of the MCP if the desired ion separation is too large. Perhaps the simplest way to deal with this is to move the MCP off of the chamber's axis by adding a curved section to the vacuum chamber. This will move the MCP into a position where it can once again collect ions. A different method of compensating for the base deflection seen by all ions is to set up an electric field perpendicular to the initial flight direction and in the plane of the ion separation. An example of such a setup in the form of a SimIon calculation is shown in Figure 14. If the plates are biased such that their electric field points in the direction opposite to that of the magnetic deflection, the ions can be re-centered on the MCP while maintaining the separation of ion species.

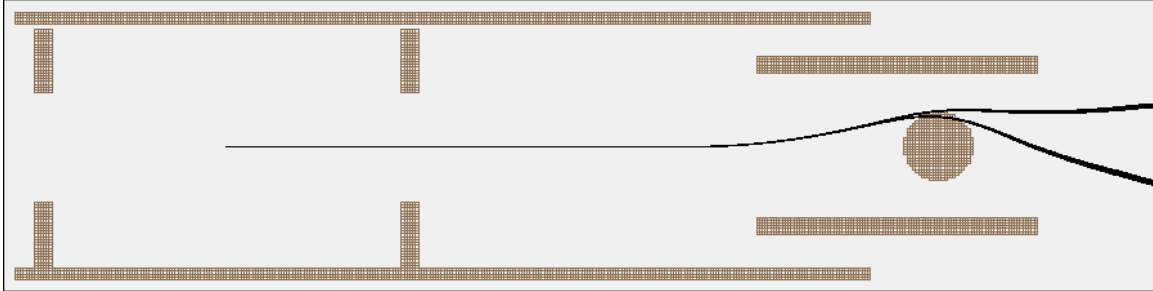


Figure 14: An example of base deflection compensation. The two electrodes surrounding the magnets bend ions in the direction opposing the magnetic deflection. This way, greater separation can be achieved while keeping the ions on the active area of the MCP.

This example adds only two plates: one grounded and the other held at a positive potential. A large advantage to this approach as opposed to moving the detector is that the amount of base deflection compensation can be varied without altering the inside of the chamber. If used in conjunction with electromagnets, the researcher will have the ability to change the injected gas, the amount of separation between species, and the amount of deflection common to all species, all without breaking vacuum. A more complex arrangement of plates could be conceived of to minimize fields outside the deflection region and reduce the spread of impact sites within a species.

4.2 Ion Optics

More work along these lines could also be done using ion optics. These are devices that manipulate ions much like photons can be manipulated using conventional optics. The ion optics equivalent of a lens is the Einzel lens. This lens is made of three tube-like electrodes: the outer two held at one potential, and the inner one held at another. Charged particles entering one end of the lens will experience an electric field gradient that causes them to drift toward the axis of the device, resulting in a focusing of the ions that is tunable to different focal lengths by varying the potential difference

between the inner and outer plates. This is shown as a SimIon simulation in Figure 15, and while the figure shows a beam of ions being focused, an Einzel lens could also be used in the experiment presented here on individual ions to reduce the impact area of each ion species. The easiest way to do this is to put it between the extraction plates and the magnet assembly.

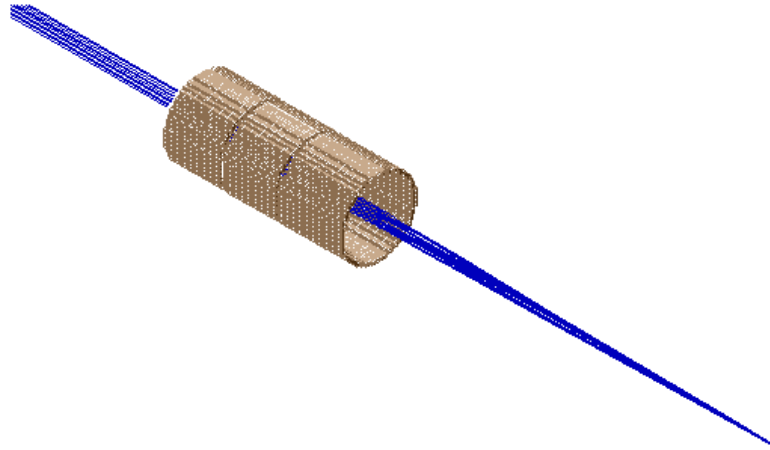


Figure 15: Einzel lens visualization produced with SimIon. Image taken from [13].

Where the Einzel lens is analogous to a conventional optics lens, the electrostatic quadrupole, shown with attached Einzel lenses in Figure 16, is the ion optics equivalent of a mirror set up for right angle reflection. It is a set of four alternately biased electrodes that are held apart to at the corners of a square. Particles that enter through a side are deflected according to their charge: neutral particles travel straight through, and oppositely charged particles are sent in opposite directions, ninety degrees from their initial trajectories. In this experiment, such a device could be used to filter out unwanted particles, should that prove to be an issue. It would also be very useful for deflecting ions by ninety degrees with minimal dispersion before they are deflected in the opposite direction by the magnet assembly. This would allow very strong magnetic deflection to be used in a straight flight tube and is a readily available alternative to the plates in Figure 14 that is designed to minimize the dispersion of the ions it deflects.

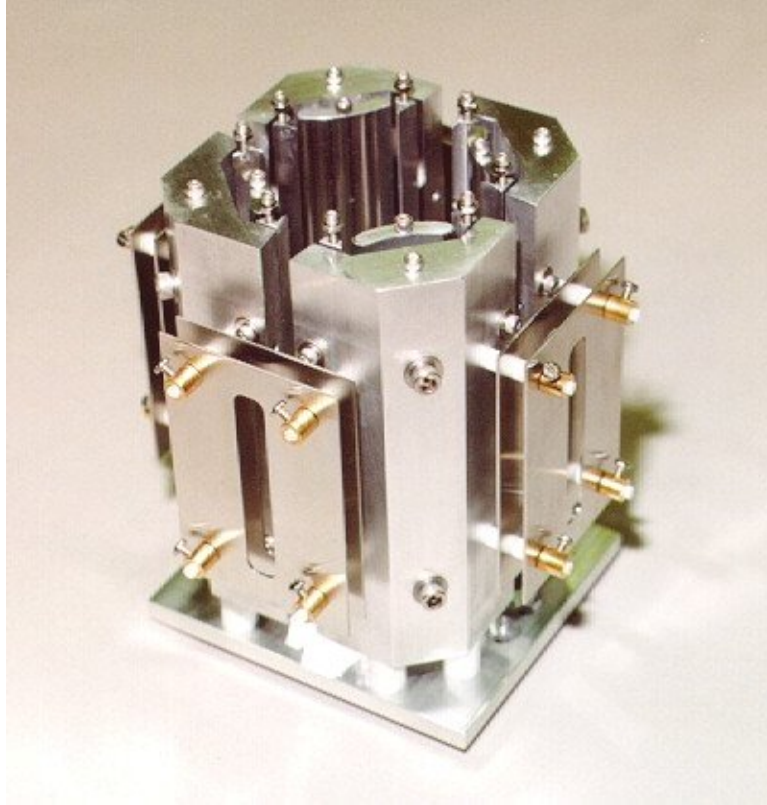


Figure 16: Electrostatic quadrupole with attached Einzel lenses to compensate for dispersion within the device. Image taken from [15].

4.3 Conclusion

Ultimately, this technique will be used at JLab's FEL, as mentioned earlier. This will allow us to take full advantage of the high repetition rate limit inherent to the spatially-resolved technique presented here. Use of the FEL will also open up the opportunity of tuning the driving field to a wide range of frequencies. Since the Keldysh parameter varies with wavelength as well as intensity, this will allow us to keep the intensity constant while observing ionization in the multiphoton and semi-classical regimes, as well as ionization in the transitional range between them.

References

- [1] R.L. Smith, Phys. Rev. **128**, 2225 (1962).
- [2] G. S. Voronov and N. B. Delone, JETP Letters **1**, 66 (1965).
- [3] P.B. Corkum, Phys. Rev. Lett. **71**, 1994 (1993).
- [4] J.L. Chaloupka, *et al.*, Optics Express **8**, 352 (2001).
- [5] <http://www.chemcool.com/elements/helium.html>, last accessed on 11/26/05.
- [6] R. Lafon, *et al.*, Phys. Rev. Lett. **86**, 2762 (2001).
- [7] Th. Weber, *et al.*, Nature **405**, 658 (2000).
- [8] J.L. Chaloupka, *et al.*, Phys. Rev. Lett. **90**, 33002 (2003).
- [9] J. Arol Simpson, Review of Scientific Instruments **35**, 1698 (1964).
- [10] C Hannay, *et al.*, Measurement Science and Technology **6**, 1140 (1995).
- [11] B. Walker, *et al.*, Phys. Rev. Lett. **73**, 1227 (1994).
- [12] <http://www.blender.org> or <http://www.blender3d.org> or <http://www.blender3d.com>,
all accessed last on 4/3/06.
- [13] <http://www.simion.com/>, last accessed on 4/3/06.
- [14] L.V. Keldysh, Zh. Eksp. Teor. Fiz. **47**, 1945 (1964) [Sov. Phys. JETP **20**, 1307
(1965)].
- [15] <http://www.apace-science.com/colutron/900h/quad.htm>, last accessed on 3/14/06.
- [16] <http://www.mumetal.com/>, last accessed on 4/20/06.